



HAL
open science

Increasing Global Terrestrial Diurnal Temperature Range for 1980-2021

Xiaowen Huang, Robert J. H. Dunn, Laurent Li, Tim R. Mcvicar, Cesar Azorin-Molina, Zhenzhong Zeng

► **To cite this version:**

Xiaowen Huang, Robert J. H. Dunn, Laurent Li, Tim R. Mcvicar, Cesar Azorin-Molina, et al.. Increasing Global Terrestrial Diurnal Temperature Range for 1980-2021. *Geophysical Research Letters*, 2023, 50, 10.1029/2023GL103503 . insu-04195510

HAL Id: insu-04195510

<https://insu.hal.science/insu-04195510>

Submitted on 4 Sep 2023

HAL is a multi-disciplinary open access archive for the deposit and dissemination of scientific research documents, whether they are published or not. The documents may come from teaching and research institutions in France or abroad, or from public or private research centers.

L'archive ouverte pluridisciplinaire **HAL**, est destinée au dépôt et à la diffusion de documents scientifiques de niveau recherche, publiés ou non, émanant des établissements d'enseignement et de recherche français ou étrangers, des laboratoires publics ou privés.



Distributed under a Creative Commons Attribution - NoDerivatives 4.0 International License

Geophysical Research Letters[®]



RESEARCH LETTER

10.1029/2023GL103503

Increasing Global Terrestrial Diurnal Temperature Range for 1980–2021

Key Points:

- The up-to-date Hadley Center Integrated Surface Database (HadISD) in-situ data reveals a reversed global diurnal air temperature range (DTR) trend, increasing for 1980–2021
- The observed spatial patterns are partially captured but the reversal trends are not shown by CMIP6 models
- The emergent constraint for CMIP6 models with HadISD estimates increasing DTR at the global scale

Supporting Information:

Supporting Information may be found in the online version of this article.

Correspondence to:

Z. Zeng,
zengzz@sustech.edu.cn

Citation:

Huang, X., Dunn, R. J. H., Li, L. Z. X., McVicar, T. R., Azorin-Molina, C., & Zeng, Z. (2023). Increasing global terrestrial diurnal temperature range for 1980–2021. *Geophysical Research Letters*, 50, e2023GL103503. <https://doi.org/10.1029/2023GL103503>

Received 28 FEB 2023
Accepted 16 MAY 2023

Xiaowen Huang¹ , Robert J. H. Dunn² , Laurent Z. X. Li³ , Tim R. McVicar^{4,5} , Cesar Azorin-Molina⁶ , and Zhenzhong Zeng¹ 

¹School of Environmental Science and Engineering, Southern University of Science and Technology, Shenzhen, China, ²Met Office Hadley Centre, Exeter, UK, ³Laboratoire de Météorologie Dynamique, Centre National de la Recherche Scientifique, Sorbonne Université, Ecole Normale Supérieure, Ecole Polytechnique, Paris, France, ⁴CSIRO Environment, Canberra, ACT, Australia, ⁵Australian Research Council Centre of Excellence for Climate Extremes, Canberra, ACT, Australia, ⁶Centro de Investigaciones sobre Desertificación, Consejo Superior de Investigaciones Científicas (CIDE, CSIC-UV-Generalitat Valenciana), Climate, Atmosphere and Ocean Laboratory (Climatoc-Lab), Valencia, Spain

Abstract The 2021 IPCC report found that most studies show declining trends for the global diurnal temperature range (DTR) since the 1950s, decreasing mainly during 1960–1980. This issue is revisited here using an up-to-date in-situ data set, Hadley Center Integrated Surface Database, constrained by rigorous station selection conditions. The global observed DTR trend was found to reverse during 1980–2021, increasing significantly at a rate of $0.091 \pm 0.008^\circ\text{C decade}^{-1}$. The trend was dominated by a faster rate of increasing daily maximum air temperature. This increasing observed trend in the past four decades was not fully captured in raw CMIP6 models, as models only partially capture the spatial patterns. With global CMIP6 outputs and regionally-available observations, the global land DTR was then estimated, through emergent constraints, to be $0.063 \pm 0.012^\circ\text{C decade}^{-1}$. The study raises concern for risks of increasing DTR globally and provides new insights into global DTR assessment.

Plain Language Summary In 2021, the IPCC reported a decrease in the near-surface diurnal air temperature range (DTR) since the 1950s. However, using the in-situ surface air temperature observations, the global DTR trend was found to reverse after the 1980s, as daily maximum air temperature increased faster than the daily minimum air temperature did between 1980 and 2021. The observed results for 1980–2014 were used to assess the historical simulations within CMIP6. Models generally depicted similar spatial variability as observed results but high variation existed between models. Most of the models did not capture the reversal of the global DTR trend and underestimated regional results. To narrow down the uncertainty and produce a complete global land DTR estimation, we applied the emergent constraint approach by combining observation data and model results. The global DTR trend from 1980 to 2014 was $0.063 \pm 0.012^\circ\text{C decade}^{-1}$. The constraining data was also used at a regional scale. It was shown that DTR trends for North America retained high uncertainty ($-0.011 \pm 0.026^\circ\text{C decade}^{-1}$), while Europe and Asia showed reduced uncertainty with increasing DTR.

1. Introduction

Diurnal temperature range (DTR), referring to the difference between the maximum and minimum near-surface air temperature within a 24-hr period, has been identified as a critical research gap in the Sixth Assessment Report (AR6) of the Intergovernmental Panel on Climate Change (IPCC, 2021). Since daily maximum and minimum temperatures are respectively mainly determined by shortwave and longwave radiation, DTR can be used to assess radiative forcing effects (Makowski et al., 2008). Tracking DTR changes allows for deeper understanding of the boundary layer dynamics, near-surface stability, and processes (e.g., the photosynthesis and respiration processes in plants) involving air temperature variability (Christy et al., 2009; Holtslag et al., 2013; Lindvall & Svensson, 2015; Peng et al., 2013). DTR is an important parameter for ecology and agriculture that affects species performance and crop yield (Lobell, 2007; Vasseur et al., 2014). It also acts as a well-known risk factor for public health, as increasing DTR is highly associated with increased mortality (Lee et al., 2018; Lim et al., 2012).

From the 1950s, in both observations and simulations, global DTR declined substantially as daily minimum air temperature increased faster than daily maximum air temperature (Lindvall & Svensson, 2015; Sun et al., 2018; Vose et al., 2005). DTR change displayed heterogeneous spatial patterns and seasonal variations (Lauritsen &

© 2023 The Authors.

This is an open access article under the terms of the [Creative Commons Attribution-NonCommercial License](https://creativecommons.org/licenses/by-nc/4.0/), which permits use, distribution and reproduction in any medium, provided the original work is properly cited and is not used for commercial purposes.

Rogers, 2012; Makowski et al., 2008; Rai et al., 2012; Vose et al., 2005). Numerous factors impact DTR and can produce complex interactions and feedbacks, which increases challenges to assess DTR changes worldwide. On the one hand, solar radiation is directly correlated with decadal DTR variability (Wang & Dickinson, 2013). Increasing cloud cover reduces DTR by reflecting shortwave radiation during the day and preventing outgoing longwave radiation at night, reducing maximum air temperature and increasing minimum air temperature (Dai et al., 1999; Roy & Balling, 2005). Greenhouse gases and aerosols contribute to the change of cloud properties, reflecting more solar radiation and thus cooling the daytime maximum temperature (Dai et al., 1997; Stjern et al., 2020). Increasing soil moisture and precipitation also reduce maximum air temperature through evaporative cooling in the daytime, especially in arid and semi-arid regions (Dai et al., 1999; Zhou et al., 2009). On the other hand, enhancing solar radiation increases DTR values (e.g., Europe; Makowski et al., 2008). Additionally, local factors (e.g., land cover changes) may also play a critical role in increasing DTR (e.g., Mexico; Englehart & Douglas, 2005).

Shortwave radiation varied significantly in the past few decades: it first decreased (global dimming) from the 1950s-to-1980s, and then began to reverse (global brightening) since the 1980s (Schwarz et al., 2020; Wild et al., 2005). During the overall period, anthropogenic emissions of greenhouse gases remained at a high level, accelerating the global warming, with the global hydrological cycle intensified and more extreme events, including droughts, floods, and heat waves (Al-Ghussain, 2019). The ongoing land use and land cover change in recent decades provided important forcing impacting the Earth system (Song et al., 2018). Under such circumstances, assessing DTR variation is challenging. Most previous studies focused on global DTR analysis for long-terms (e.g., from the 1950s to present) but few investigated the near-term DTR trends (e.g., since the 1980s; Braganza et al., 2004; Zhou et al., 2009; Sun et al., 2018). Recent near-term DTR studies are limited to a regional scale (Feng et al., 2018; Yang & Ren, 2017), and research on a global scale is seldom performed (Rohde et al., 2013; Sun et al., 2018). In the last IPCC report, the major conclusion drawn from the near-term DTR analysis mainly covered the period before 2004 due to data availability (IPCC, 2021; Thorne et al., 2016). Therefore, it is critical to assess global DTR trends using up-to-date datasets.

Currently, global analysis based on observational station data is limited by the spatial data coverage due to the quality and completeness of the long-term station records. Missing records have led to large gaps in South America, Africa, and areas at the North Pole where stations fail to pass selection criteria (Sun et al., 2018; Thorne et al., 2016; Vose et al., 2005). DTR investigations in these regions are generally performed using gridded interpolation. Another approach for a complete global land study is numerical simulation. However, in numerical studies, simulated DTR results have high discrepancies between models and the values are generally underestimated when compared with observed mean DTR values (Sun et al., 2018), probably resulting from deficiencies of modeling cloud and aerosol effects (Lindvall & Svensson, 2015). To fill these research gaps, we analyzed global observational DTR trends for 1980–2021 using the up-to-date in-situ Hadley Center Integrated Surface Database (HadISD) data set. The observed results between 1980 and 2014 (limited by CMIP6 historical period) are applied to assess the simulated DTR trends from CMIP6 historical outputs. The discrepancies between the two results are investigated and discussed. We combine model outputs and the in-situ data set using the emergent constraint approach and estimate the global complete land DTR trends for 1980–2014.

2. Materials and Methods

We use the in-situ sub-daily HadISD data set (version 3.3.0.202205p) developed by the UK Met Office Hadley Center (Dunn, 2019; Dunn et al., 2012, 2016). HadISD is based on the ISD data set (Smith et al., 2011), developed by NOAA's National Climatic Data Center. This version of the HadISD contains 9,555 station-observed time series since 1 January 1931 for numerous variables, including air temperature, wind speed, and sea level pressure, with at least 4 observations per day (reporting from 6-hourly to hourly). Various quality control procedures have been applied to the data set, including duplicate checks, distribution gap checks, and climatological outlier checks (Dunn et al., 2012, 2016).

We adopt strict station selection criteria. For all stations, a day is declared valid if there are at least 5 observations (excluding 6-hourly observations for more precise results), otherwise, it is identified as a missing day. Based on the WMO standard practices, a month is discarded if there are more than 11 missing days overall or 5 or more consecutive days are missing (WMO, 2017). For the 1980–2021 period, only stations with less or equal to 5 missing months are retained, such that the missing rate is smaller than 1% (5 of 504 months). After selection, 1,571

stations are retained in the analysis. They are mainly located in the United States of America, Europe, China, and Japan, with poor coverage in South America, Africa, Australia, and central Russia (Figure S1 in Supporting Information S1). The selection results in temporal resolution of 3-hourly and hourly, with observed times evenly distributed within the day (Figure S2 in Supporting Information S1). For each station, we first calculate the monthly mean DTR from the valid days in the month. We then derive the annual mean DTR based on monthly values. The station-based values are finally averaged onto $5^\circ \times 5^\circ$ grid cells, with at least one station available in each grid, following Vose et al. (2005) and Sun et al. (2018). For the conservation purpose in a latitude-longitude coordinate system, grid values are weighted by the cosine of latitude at the central point of each grid. Finally, we construct the global and regional annual time series by averaging all area-weighted variables of all grids. The linear trends are determined by the least-squares method. The t -test is applied to examine the significance at $\alpha = 0.05$. The above procedures are also applied to the regional trend analysis.

Due to the limited coverage of meteorological stations given our strict selection criteria, we process the emergent constraint approach to further assess the range of global DTR trends, including all land areas with and without observation records (Eyring et al., 2019). The emergent constraint integrates two diagnostic variables across model ensembles, within which one can be compared with observational data and the other cannot (Wang et al., 2020). The method has reduced uncertainties for land-atmospheric interactions modeling and has been widely used (Chai et al., 2022; Cox et al., 2018; Wang et al., 2020). Here, we use HadISD observations to constrain CMIP6 model outputs. We obtain the daily maximum and minimum near-surface air temperature from all available CMIP6 historical simulations (35 models in total) of variant label “r1i1p1f1”, with detailed descriptions displayed in Table S1 in Supporting Information S1. Since historical runs cover the 1850–2014 period, the emergent constraint approach for our DTR analysis is set for 1980–2014. All models are re-gridded to $5^\circ \times 5^\circ$ grid cells to correspond to the observation grids and the DTR values are calculated. We then compute area-weighted linear DTR trends of grids with HadISD observed data available (HadISD grids) and the area-weighted linear DTR trends of all land grids for each model. The linear relationship between two series of trends is defined following Cox et al. (2018).

$$f_n = a + bx_n, \quad (1)$$

$$\bar{b} = \frac{\sum_{n=1}^N (x_n - \bar{x})(y_n - \bar{y})}{\sum_{n=1}^N (x_n - \bar{x})^2}, \quad (2)$$

where f_n denotes the linear regression between series of DTR trends of HadISD grids (x_n) and series of DTR trends of global grids (y_n , $1 \leq n \leq 35$), a and b represent the intercept and gradient, respectively. N denotes the total data points and \bar{x} and \bar{y} represents the average of x_n and y_n , respectively. The prediction error (σ_f) is calculated as:

$$\sigma_f = s \sqrt{1 + \frac{1}{N} + \frac{(x_n - \bar{x})^2}{\sum_{n=1}^N (x_n - \bar{x})^2}}, \quad (3)$$

where s is calculated from the estimation of the variance (s^2) in $y_n - f_n$:

$$s^2 = \frac{1}{N-2} \sum_{n=1}^N (y_n - f_n)^2, \quad (4)$$

The probability density function (PDF) of y given x ($P(y|x)$) is:

$$P(y|x) = \frac{1}{\sqrt{2\pi\sigma_f^2}} e^{-\frac{(y-f(x))^2}{2\sigma_f^2}}, \quad (5)$$

Similarly, the PDF for observed HadISD trend $P(x)$ also follows the Gaussian distribution. The PDF after emergent constraint ($P(y)$) is:

$$P(y) = \int_{-\infty}^{\infty} P(y|x)P(x)dx, \quad (6)$$

The constrained global DTR trend and the uncertainty are then derived from $P(y)$.

3. Results

3.1. Observed DTR Trends

While most of the DTR declines occurred between 1960 and 1980 (Thorne et al., 2016), the DTR values increase since the 1980s using the observation-based HadISD data set, suggesting that the global DTR trend has reversed for recent decades (Figure S3 in Supporting Information S1). This is the result of 1980–2021 maximum air temperature increasing at $0.344 \pm 0.025^\circ\text{C decade}^{-1}$, whereas minimum air temperature, although also increasing, progress at a lower rate of $0.254 \pm 0.025^\circ\text{C decade}^{-1}$. Together they result in an increase of DTR of $0.091 \pm 0.008^\circ\text{C decade}^{-1}$. Different magnitudes in the changes of maximum air temperature and minimum air temperature are also identified spatially (Figure S4 in Supporting Information S1). Increases in maximum air temperature are detected worldwide, with only a few exceptions in South America (Figure S4a in Supporting Information S1). Minimum air temperature shows similar patterns of increase as maximum air temperature, but opposite trends are identified in South America and southern Africa (Figure S4b in Supporting Information S1). The changes in DTR have high spatial variability worldwide (Figure 1a). Significant ($p < 0.05$) DTR increases are observed in the western United States, Europe, South Africa, and western Asia. Regionally, high DTR trends in Europe and Asia ($0.199 \pm 0.014^\circ\text{C decade}^{-1}$ and $0.096 \pm 0.012^\circ\text{C decade}^{-1}$, respectively) are mainly responsible for the global trends (Figures 1b, 1d, and 1e). The DTR trend for North America is weak and not significant ($p > 0.05$; Figure 1c).

3.2. Assessment of Model-Simulated DTR Trends

The CMIP6 model performance is first assessed inter-models globally. Overall, the CMIP6 models agree with the conclusion that global DTR decline between 1980 and 2014, with a mean significant trend of $-0.019 \pm 0.001^\circ\text{C decade}^{-1}$ for global land grids (Figure 2a). For the 33 models with decreasing trends, 78.8% of the models report declining DTR trends less than $-0.03^\circ\text{C decade}^{-1}$ (26 models; Figure 2b). Only 2 models show small magnitudes of increasing trends ($<0.01^\circ\text{C decade}^{-1}$), namely NorCPM1 and NorESM2-MM. Despite the high model agreement in temporal trends, models display rather large variations in average spatial DTR trends and inter-model comparison (Figure S5 in Supporting Information S1 and Figure 2c). The spatial pattern for average DTR trends of 35 CMIP6 models during 1980–2014 is highly heterogeneous. The areas of increase are mainly located in part of subtropical to temperate regions in the northern hemisphere (30°N – 55°N) and tropical to sub-tropical regions in the southern hemisphere (10°S – 30°S), such as United States, Europe, South America, and Australia, while decreases are found mainly in tropical, boreal and part of sub-tropical regions, including Asia, northern North America, and large parts of Africa (Figure S5 in Supporting Information S1). Models largely agree on the decreasing DTR values in central Africa and in boreal high-latitude regions. High consistency in increasing DTR is found mainly in southern Europe, eastern United States, and eastern Australia. However, large model discrepancies still exist between regions. Models display an agreement of less than 70% in western Canada, western Australia, and especially large parts of Asia and South America. The overall inconsistency indicates high model uncertainties worldwide.

The model performance is further evaluated by the observed results during 1980–2014, only considering the model grids with HadISD data available (grids shown in Figure 1a). Though showing high uncertainties spatially, models still produce similar patterns as the observed results, mainly in western United States, South America, Europe, and Japan (Figures 1a and 2c, and Figure S6 in Supporting Information S1). For temporal trends, we find that the trends in observational data are not fully captured by the CMIP6 models. For all grids with observed HadISD data, over 60% of models show decreasing DTR (24 models), which contrasts with the observed trends ($0.112 \pm 0.010^\circ\text{C decade}^{-1}$; Figure 3a). Though the other 11 models capture the increasing DTR, the trends are all underestimated, with magnitudes of less than $0.02^\circ\text{C decade}^{-1}$. Regionally, in North America, both the HadISD data set and the models show high uncertainty. Fifteen models displayed declining DTR values while the other 20 models show the opposite (Figure 3b). The HadISD data set shows no significant trend ($0.006 \pm 0.032^\circ\text{C decade}^{-1}$, $p > 0.05$). Twenty four out of thirty five models agreed with the increasing DTR in HadISD over Europe but underestimated the magnitude by over half, as the maximum trend is measured to be $0.085 \pm 0.030^\circ\text{C decade}^{-1}$ and the observed trend is in the range $0.205 \pm 0.019^\circ\text{C decade}^{-1}$ (Figure 3c). The

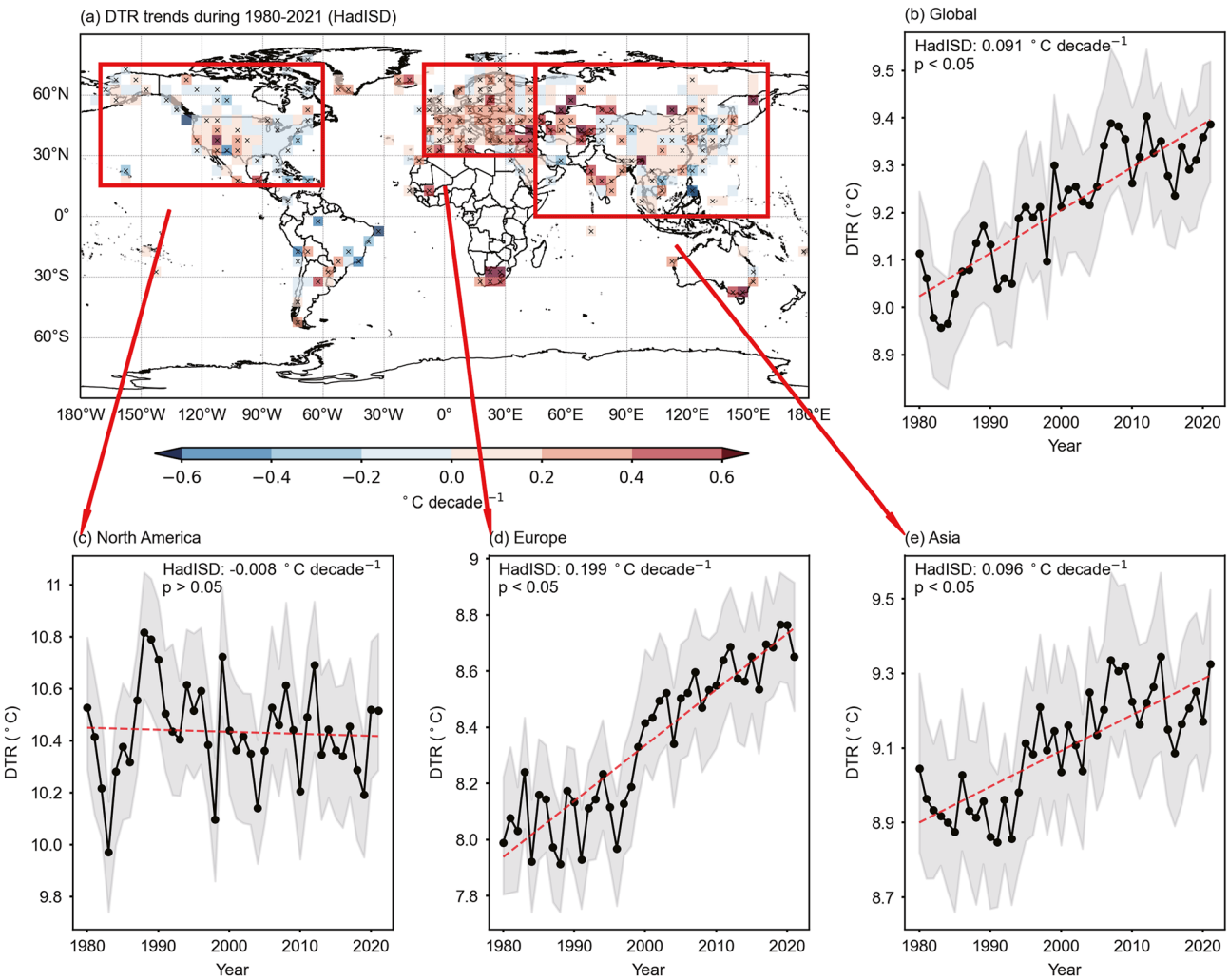


Figure 1. Spatial distribution and temporal DTR trends from HadISD observations. (a) Global spatial distribution of linear trend of annual DTR, 1980–2021. Black crosses denote a significant trend with $p < 0.05$. The red polygons outline North America, Europe, and Asia, respectively. Annual DTR trends during 1980–2021 in the HadISD data set (black line) are shown for (b) global, (c) North America, (d) Europe, and (e) Asia. In (b) to (e) the red line is the line of best fit of the time series, and the slope and probability statistics of that line are shown in black text on each sub-plot. The gray shadings denote the uncertainty calculated as the interquartile range of the results by randomly selecting 40% of the grids and repeating 300 times. North America is defined by the opposing rectangle corners being 170°W, 75°N and 60°W, 15°N. For Europe these locations are 10°W, 75°N and 45°E, 30°N, for Asia they are 45°E, 75°N and 160°E, 0°N.

largest disparity lies in Asia, as nearly all models (32 of 35) show decreases in DTR but HadISD shows reversed trends ($0.124 \pm 0.014^\circ\text{C decade}^{-1}$; Figure 3d). Only 3 models capture the increasing trends, but with magnitudes below $0.02^\circ\text{C decade}^{-1}$.

3.3. Emergent Constraint for Complete Global and Regional DTR Trends

Through the assessment, we find that models have high agreement temporally but are less likely to capture the reversal trends, and depict part of the spatial pattern generally well but with high inter-model variation. This implies that although model simulations provide results over the complete global land area, models alone are unable to replicate accurate measurements. Therefore, the global DTR trends are further investigated through emergent constraints (Figure 4a). The model grids with HadISD data (denoted “HadISD grids” herein) experience larger magnitudes of DTR change than all model grids (termed “global grids” herein). The temporal trends for most of the models (24 of 35) decrease for both HadISD grids and global grids, and some (9 of 35) display contrasting trends, meaning an increase in HadISD grids but decrease in global grids. Few models (2 of 35) show consistently increasing trends in HadISD and global grids. Regardless of the large variation, the linear fit of the

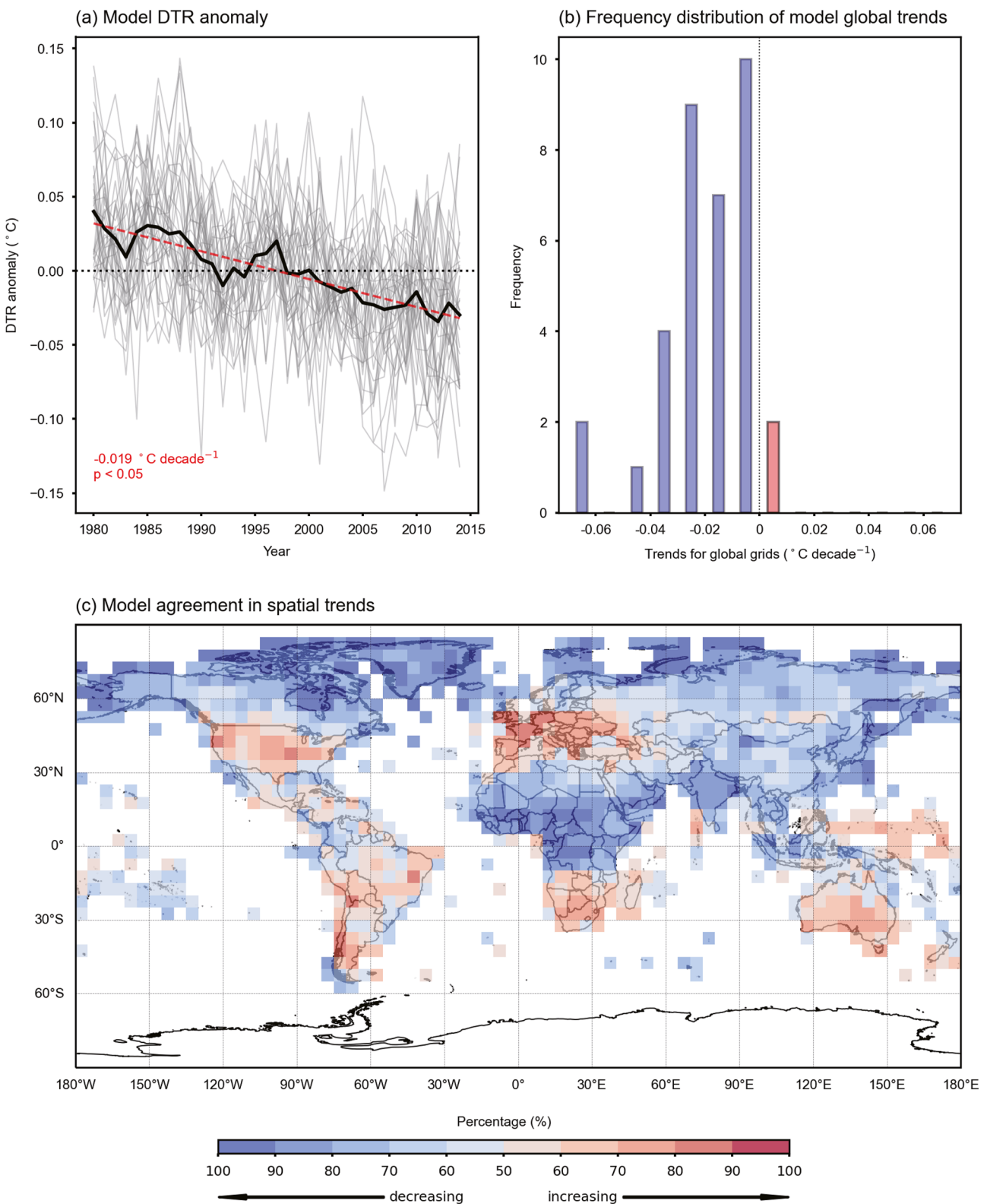


Figure 2. Global DTR trends and agreement among models. (a) Annual DTR anomaly of the 35 CMIP6 models. The gray lines represent DTR anomaly for each model and the black line denote the mean for all models. The red line is the line of best fit of the mean of all models, and the slope and probability statistics of that line are shown in red text in the bottom-left corner. (b) Frequency distribution of global DTR trends ($^{\circ}\text{C decade}^{-1}$) for the 35 CMIP6 models during 1980–2014. The blue (red) bars denote model trends less (greater) than zero. (c) Percentage of models showing increasing (decreasing) DTR trends in each 5° by 5° grid.

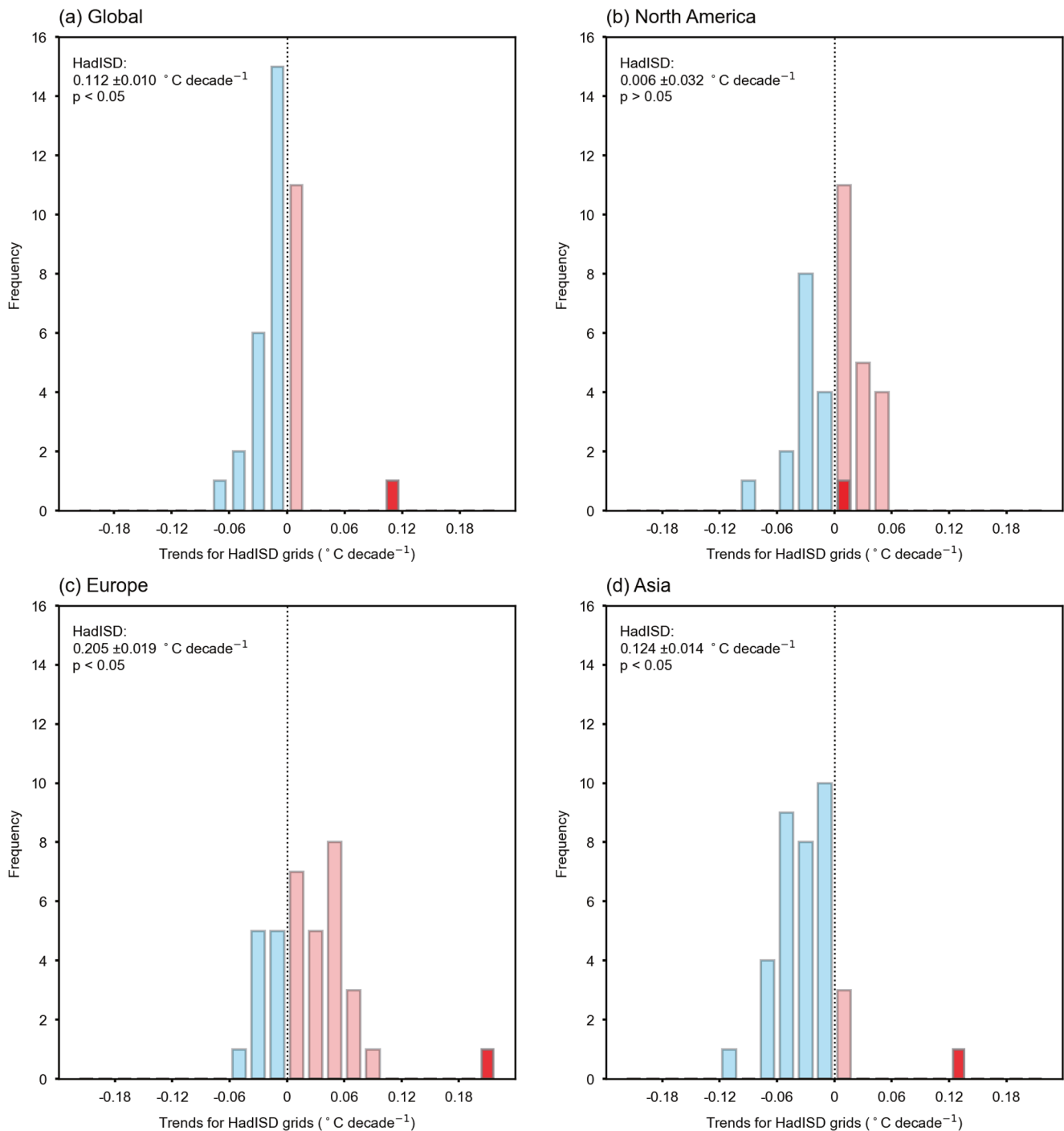


Figure 3. Frequency distribution of simulated DTR trends for HadISD grids shown in Figure 1(a) and the corresponding DTR trends in the observed HadISD data set (red bar) in (a) global, (b) North America, (c) Europe, and (d) Asia. The blue (light red) bars denote negative (positive) model trends. Data provided in the top-left of each sub-part refers to the values of the observed HadISD DTR trend (as shown by the red bar). The three geographic regions are defined in Figure 1 caption.

two trends for different models agrees well with an R-squared value of 0.78. The trend of global land is then estimated to be $0.063 \pm 0.012 \text{ } ^\circ\text{C decade}^{-1}$ according to the linear fit set by models (Figure 4b). The results suggest that global DTR experiences a reversal of trends in the recent decades (1980–2014), decreasing from the 1950s to the 1980s whereas from 1980 to 2014 the DTR trend is increasing. The reversal trends are not only restricted to lands with HadISD observations, they also extend to most of the CMIP6-based simulated global lands.

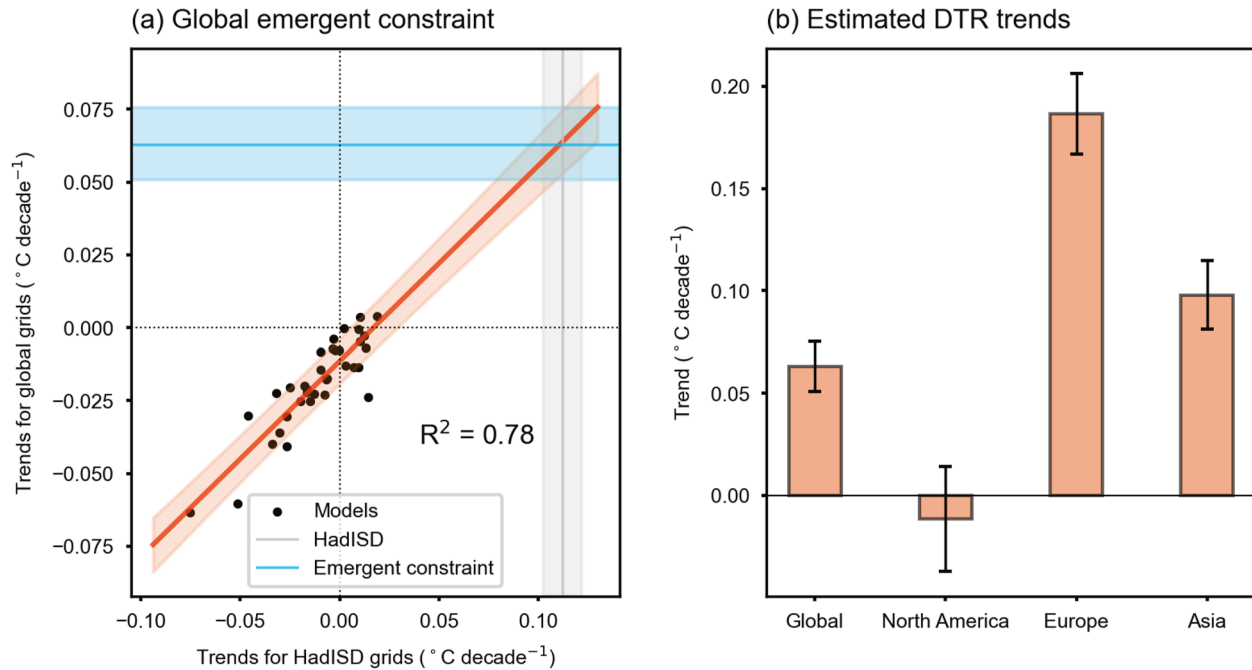


Figure 4. Emergent constraint approach. (a) The emergent relationship between trends of grids for global land and trends of grids with observed data for 1980–2014. The orange solid line shows the linear regression with prediction error (orange shading) and the gray vertical solid line denotes the trend of HadISD data during 1980–2014 and one standard deviation (gray shading). The horizontal blue solid line shows the best estimation and blue shading shows the uncertainty for trends of global land. (b) The estimated DTR trends through emergent relationship globally and regionally. Error bars indicate the estimation of \pm one standard deviation. The three geographic regions are defined in Figure 1 caption.

The emergent relationship is also adopted on regional DTR trend estimation in North America, Europe, and Asia, as there still exist $5^\circ \times 5^\circ$ grids cells in each region without HadISD observations (Figure 4b). The high spatial variation between western and eastern North America leads to large uncertainty there, revealed by both models and HadISD data (Figure 1a and Figure S7a in Supporting Information S1). The missing observed areas of North America are mainly in Canada and Mexico (Figure 1a). When the model constraint method is employed, the North American DTR trend is estimated to be $-0.011 \pm 0.026^\circ\text{C decade}^{-1}$ (Figure 4b). In Europe, the HadISD stations cover nearly all land grids (Figure 1a), which produces a high correlation between trends for HadISD grids and trends for land grids (Figure S7b in Supporting Information S1). Therefore, the model estimation reveals little difference in the observational trends, at the value of $0.187 \pm 0.020^\circ\text{C decade}^{-1}$ (Figure 4b). In Asia, large areas in Russia, parts of central Asia, and north India exist with no HadISD observations (Figure 1a). Models produce a high correlation ($R^2 = 0.87$), which made the assessment more applicable (Figure S7c in Supporting Information S1). The trend is estimated to be $0.098 \pm 0.017^\circ\text{C decade}^{-1}$ (Figure 4b), smaller than the European DTR trends, but still shows a strong increase. Overall, the emergent constraint provides right-shifted results with reduced uncertainty (Figure S8 in Supporting Information S1).

4. Discussion

Thorne et al. (2016) reported a non-significant trend in global DTR since 1979 and showed inter-data set disagreement. Here we find that global DTR has reversed from decreasing to increasing during the past four decades using the HadISD data set. We are aware that being a sub-daily data set, the DTR for each station may be affected by the increasing observation frequency, since the DTR may be underestimated in the past but more accurately measured more recently as the observation frequency increases. Therefore, we test another method (“fixed hour method”) to eliminate the potential effect. For each station, we note the observation times available in 1980 and depict the mean diurnal air temperature cycle for 1980–2021 only using these times. Then we determine the hours of maximum air temperature (Tmax hour) and minimum air temperature (Tmin hour) of these periods. The “valid day” is then determined if both the Tmax hour and Tmin hour are available. The daily DTR is calculated as the difference of the values of Tmax hour and Tmin hour. As shown in Figure S9a in Supporting Information S1, the

true DTR could be underestimated due to less reporting periods (e.g., 3-hr period), but as we keep the Tmax hour and Tmin hour fixed, the change of measured DTR reflected the change of true DTR (Figures S9b and S9c in Supporting Information S1). Generally, the two methods display similar spatial patterns (Figure S9d in Supporting Information S1). Although the “fixed hour method” shows a smaller magnitude of DTR trends (Figure S9e in Supporting Information S1), the mean global DTR still shows increasing results.

The increasing DTR has been reported by Rohde et al. (2013) using the Berkeley data set, and also mentioned as faster rate of increasing maximum air temperature by Dunn et al. (2019) using HadISD over 1973–2018. Now we further confirm the increasing trend in the past four decades. The global spatial patterns of DTR from HadISD are consistent with the patterns of Berkeley and HadGHCND datasets in Thorne et al. (2016). Our results are further proved by using the Berkeley data set over 1980–2021 (Figure S10 in Supporting Information S1). Regional patterns of North America and Europe also corroborate a number of studies using different datasets (Thorne et al., 2016; Vose et al., 2005), such as HadEX2 (Donat et al., 2013a), GHCNDEX (Donat et al., 2013b), and CMA-LSAT (Sun et al., 2018). Compared with the datasets showing global decreasing DTR, the largest discrepancies are found in Asia. Increased DTR in southeastern China (Yang & Ren, 2017), south India (Kothawale et al., 2012), and central Asia (Feng et al., 2018) have been previously observed. Recent research has concluded several potential factors responsible for increasing DTR trends. Increasing surface solar radiation globally since the 1980s, in which aerosol and greenhouse gases have played a crucial role, has increased the DTR (Wild et al., 2007; Makowski et al., 2008; Kothawale et al., 2012). The transition from solar dimming to brightening is more evident in recent years in China (Wang & Wild, 2016; Yang et al., 2019), which may explain the increasing DTR in Asia. Moreover, the reduction of cloud cover and water vapor leads to limited precipitation, all of which combined with the gradual brightening are believed to be major explanations for the DTR increase in Asia (Feng et al., 2018; Wang & Wild, 2016; Yang & Ren, 2017). Land cover change in China, for example, grassland degradation, may also be a factor of increasing DTR (Shen et al., 2017).

Several studies have reported underestimation and discrepancies of simulated DTR trends in models compared to observational data (Lewis & Karoly, 2013; Sillmann et al., 2013). The discrepancies still exist in our analysis of CMIP6 models, with HadISD observations (increasing, Figure 2b) and CMIP6 models (decreasing, Figure 1a) providing contrasting 1980–2014 DTR trends. Our finding is consistent with previous studies (Fan et al., 2020; Wang & Clow, 2020). The simulated solar radiation is probably the most crucial factor for DTR discrepancies. The increased DTR before the 1950s also fails to be captured since models simulate declining solar radiation while the observed records increase, which leads to less warming of maximum air temperature, therefore displaying decreased simulated DTR (Wang & Clow, 2020). As global brightening continues, the deficiencies of radiation simulation may be one of the major reasons to explain the contradictory DTR trends between models and observations. Anthropogenic forcing influences DTR trends by changing clouds, land surface processes, and radiative fluxes, but accurate representations of these forcing largely failed in models (Lewis & Karoly, 2013; Zhou et al., 2010).

Due to the current limitation of model's simulation of DTR, use of the emergent relationship to constrain DTR trend appears to be useful for its comprehensive estimation and for narrowing uncertainties. Reducing uncertainties enables models to be better improved through more accurate evaluations (Brient, 2020), and may also allow a more efficient adaptation planning toward increasing DTR (Williamson et al., 2021). The use of high-quality observation data set with rigorous selection criteria maintains the continuity of time series, preserving the original trends for each station, improving the accuracy of a global assessment. The reverse DTR trends are now observed globally in the context of global brightening. As the world population keeps rising, the increase of DTR may provide greater risks to human beings, raising the precaution of increasing mortality (United Nations, 2022). The emergent constraint approach is not only limited to DTR assessment but also applicable on other climate indicators that fail to be well-captured by the current suite of models.

5. Conclusion

The DTR trends since the 1980s are investigated through the up-to-date HadISD observational data set. Observational data shows a reversed global trend, increasing for 1980–2021. This reversal is not captured by most of the CMIP6 models globally and regionally in North America, Europe and Asia. The observed spatial variability is partially depicted by models but with high inter-model disagreement. To offer a complete global land DTR assessment, the emergent constraint approach used observational data to constrain the CMIP6 model simulated

DTR. The DTR trends during 1980–2014 were estimated to be $0.063 \pm 0.012^{\circ}\text{C decade}^{-1}$ globally. Regionally, the estimated DTR for North America decreased with high uncertainty, while Europe and Asia showed increasing DTR with lower uncertainty. The study reveals the global DTR reversal, from declining to increasing in recent decades, which may raise concerns about the potential influence on ecology and human health from DTR increase. The approach of emergent constraint provides new insights and serves as a reference for the global assessment of climate indicators.

Conflict of Interest

The authors declare no conflicts of interest relevant to this study.

Data Availability Statement

The HadISD dataset can be retrieved from <https://www.metoffice.gov.uk/hadobs/hadis/> (last accessed 28 February 2023; Dunn, 2019). The CMIP6 model outputs are available at <https://esgf-node.llnl.gov/search/cmip6/> (last accessed 28 February 2023).

Acknowledgments

This study was supported by the National Natural Science Foundation of China (42071022), the start-up fund provided by the Southern University of Science and Technology (29/Y01296122), and Highlight Project on Water Security and Global Change of the Southern University of Science and Technology (G02296302). Robert J. H. Dunn was supported by the Met Office Hadley Centre Climate Programme funded by BEIS and by the UK-China Research & Innovation Partnership Fund through the Met Office Climate Science for Service Partnership (CSSP) China as part of the Newton Funds. Laurent Li acknowledged French GENCI for allocation of computing resources.

References

- Al-Ghussain, L. (2019). Global warming: Review on driving forces and mitigation. *Environmental Progress & Sustainable Energy*, 38(1), 13–21. <https://doi.org/10.1002/ep.13041>
- Braganza, K., Karoly, D. J., & Arblaster, J. M. (2004). Diurnal temperature range as an index of global climate change during the twentieth century. *Geophysical Research Letters*, 31(13), L13217. <https://doi.org/10.1029/2004GL019998>
- Brient, F. (2020). Reducing uncertainties in climate projections with emergent constraints: Concepts, examples and prospects. *Advances in Atmospheric Sciences*, 37, 1–15. <https://doi.org/10.1007/s00376-019-9140-8>
- Chai, Y., Yue, Y., Slater, L. J., Yin, J., Borthwick, A. G., Chen, T., & Wang, G. (2022). Constrained CMIP6 projections indicate less warming and a slower increase in water availability across Asia. *Nature Communications*, 13(1), 4124. <https://doi.org/10.1038/s41467-022-31782-7>
- Christy, J. R., Norris, W. B., & McNider, R. T. (2009). Surface temperature variations in East Africa and possible causes. *Journal of Climate*, 22(12), 3342–3356. <https://doi.org/10.1175/2008JCLI2726.1>
- Cox, P. M., Huntingford, C., & Williamson, M. S. (2018). Emergent constraint on equilibrium climate sensitivity from global temperature variability. *Nature*, 553(7688), 319–322. <https://doi.org/10.1038/nature25450>
- Dai, A., Genio, A. D. D., & Fung, I. Y. (1997). Clouds, precipitation and temperature range. *Nature*, 386(6626), 665–666. <https://doi.org/10.1038/386665b0>
- Dai, A., Trenberth, K. E., & Karl, T. R. (1999). Effects of clouds, soil moisture, precipitation, and water vapor on diurnal temperature range. *Journal of Climate*, 12(8), 2451–2473. [https://doi.org/10.1175/1520-0442\(1999\)012<2451:EOCSMP>2.0.CO;2](https://doi.org/10.1175/1520-0442(1999)012<2451:EOCSMP>2.0.CO;2)
- Donat, M. G., Alexander, L. V., Yang, H., Durre, I., Vose, R., & Caesar, J. (2013b). Global land-based datasets for monitoring climatic extremes. *Bulletin of the American Meteorological Society*, 94(7), 997–1006. <https://doi.org/10.1175/BAMS-D-12-00109.1>
- Donat, M. G., Alexander, L. V., Yang, H., Durre, I., Vose, R., Dunn, R. J., et al. (2013a). Updated analyses of temperature and precipitation extreme indices since the beginning of the twentieth century: The HadEX2 dataset. *Journal of Geophysical Research: Atmospheres*, 118(5), 2098–2118. <https://doi.org/10.1002/jgrd.50150>
- Dunn, R. J., Willett, K. M., & Parker, D. E. (2019). Changes in statistical distributions of sub-daily surface temperatures and wind speed. *Earth System Dynamics*, 10(4), 765–788. <https://doi.org/10.5194/esd-10-765-2019>
- Dunn, R. J., Willett, K. M., Parker, D. E., & Mitchell, L. (2016). Expanding HadISD: Quality-controlled, sub-daily station data from 1931 [Dataset]. Geoscientific Instrumentation, Methods and Data Systems, 5(2), 473–491. <https://doi.org/10.5194/gi-5-473-2016>
- Dunn, R. J., Willett, K. M., Thorne, P. W., Woolley, E. V., Durre, I., Dai, A., et al. (2012). HadISD: A quality-controlled global synoptic report database for selected variables at long-term stations from 1973–2011. *Climate of the Past*, 8(5), 1649–1679. <https://doi.org/10.5194/cp-8-1649-2012>
- Dunn, R. J. H. (2019). HadISD version 3: Monthly updates. *Hadley Centre Technical Note*, 103, 1–10.
- Engelhart, P. J., & Douglas, A. V. (2005). Changing behavior in the diurnal range of surface air temperatures over Mexico. *Geophysical Research Letters*, 32(1), L01701. <https://doi.org/10.1029/2004GL02113>
- Eyring, V., Cox, P. M., Flato, G. M., Gleckler, P. J., Abramowitz, G., Caldwell, P., et al. (2019). Taking climate model evaluation to the next level. *Nature Climate Change*, 9(2), 102–110. <https://doi.org/10.1038/s41558-018-0355-y>
- Fan, X., Miao, C., Duan, Q., Shen, C., & Wu, Y. (2020). The performance of CMIP6 versus CMIP5 in simulating temperature extremes over the global land surface. *Journal of Geophysical Research: Atmospheres*, 125(18), e2020JD033031. <https://doi.org/10.1029/2020JD033031>
- Feng, R., Yu, R., Zheng, H., & Gan, M. (2018). Spatial and temporal variations in extreme temperature in Central Asia. *International Journal of Climatology*, 38, e388–e400. <https://doi.org/10.1002/joc.5379>
- Holtslag, A. A. M., Svensson, G., Baas, P., Basu, S., Beare, B., Beljaars, A. C. M., et al. (2013). Stable atmospheric boundary layers and diurnal cycles: Challenges for weather and climate models. *Bulletin of the American Meteorological Society*, 94(11), 1691–1706. <https://doi.org/10.1175/BAMS-D-11-00187.1>
- IPCC. (2021). *Climate change 2021: The physical science basis. Contribution of working Group I to the Sixth assessment report of the intergovernmental Panel on climate change* (pp. 2391). Cambridge University Press. <https://doi.org/10.1017/9781009157896>
- Kothawale, D. R., Kumar, K. K., & Srinivasan, G. (2012). Spatial asymmetry of temperature trends over India and possible role of aerosols. *Theoretical and Applied Climatology*, 110(1), 263–280. <https://doi.org/10.1007/s00704-012-0628-8>
- Lauritsen, R. G., & Rogers, J. C. (2012). US diurnal temperature range variability and regional causal mechanisms, 1901–2002. *Journal of Climate*, 25(20), 7216–7231. <https://doi.org/10.1175/JCLI-D-11-00429.1>

- Lee, W., Kim, Y., Honda, Y., & Kim, H. (2018). Association between diurnal temperature range and mortality modified by temperature in Japan, 1972–2015: Investigation of spatial and temporal patterns for 12 cause-specific deaths. *Environment International*, *119*, 379–387. <https://doi.org/10.1016/j.envint.2018.06.020>
- Lewis, S. C., & Karoly, D. J. (2013). Evaluation of historical diurnal temperature range trends in CMIP5 models. *Journal of Climate*, *26*(22), 9077–9089. <https://doi.org/10.1175/JCLI-D-13-00032.1>
- Lim, Y. H., Park, A. K., & Kim, H. (2012). Modifiers of diurnal temperature range and mortality association in six Korean cities. *International Journal of Biometeorology*, *56*(1), 33–42. <https://doi.org/10.1007/s00484-010-0395-0>
- Lindvall, J., & Svensson, G. (2015). The diurnal temperature range in the CMIP5 models. *Climate Dynamics*, *44*(1), 405–421. <https://doi.org/10.1007/s00382-014-2144-2>
- Lobell, D. B. (2007). Changes in diurnal temperature range and national cereal yields. *Agricultural and Forest Meteorology*, *145*(3–4), 229–238. <https://doi.org/10.1016/j.agrformet.2007.05.002>
- Makowski, K., Wild, M., & Ohmura, A. (2008). Diurnal temperature range over Europe between 1950 and 2005. *Atmospheric Chemistry and Physics*, *8*(21), 6483–6498. <https://doi.org/10.5194/acp-8-6483-2008>
- Peng, S., Piao, S., Ciais, P., Myneni, R. B., Chen, A., Chevallier, F., et al. (2013). Asymmetric effects of daytime and night-time warming on Northern Hemisphere vegetation. *Nature*, *501*(7465), 88–92. <https://doi.org/10.1038/nature12434>
- Rai, A., Joshi, M. K., & Pandey, A. C. (2012). Variations in diurnal temperature range over India: Under global warming scenario. *Journal of Geophysical Research*, *117*(D2), D02114. <https://doi.org/10.1029/2011JD016697>
- Rohde, R., Muller, R. A., Jacobsen, R., Muller, E., Perlmutter, S., Rosenfeld, A., et al. (2013). A new estimate of the average Earth surface land temperature spanning 1753 to 2011. *Geoinfor Geostat: An Overview*, *1*, 1. <https://doi.org/10.4172/2327-4581.1000101>
- Roy, S. S., & Balling, R. C., Jr. (2005). Analysis of trends in maximum and minimum temperature, diurnal temperature range, and cloud cover over India. *Geophysical Research Letters*, *32*(12), L12702. <https://doi.org/10.1029/2004GL022201>
- Schwarz, M., Folini, D., Yang, S., Allan, R. P., & Wild, M. (2020). Changes in atmospheric shortwave absorption as important driver of dimming and brightening. *Nature Geoscience*, *13*(2), 110–115. <https://doi.org/10.1038/s41561-019-0528-y>
- Shen, X., Liu, B., & Lu, X. (2017). Effects of land use/land cover on diurnal temperature range in the temperate grassland region of China. *Science of the Total Environment*, *575*, 1211–1218. <https://doi.org/10.1016/j.scitotenv.2016.09.187>
- Sillmann, J., Kharin, V. V., Zhang, X., Zwiers, F. W., & Bronaugh, D. (2013). Climate extremes indices in the CMIP5 multimodel ensemble: Part 1. Model evaluation in the present climate. *Journal of Geophysical Research: Atmospheres*, *118*(4), 1716–1733. <https://doi.org/10.1002/jgrd.50203>
- Smith, A., Lott, N., & Vose, R. (2011). The integrated surface database: Recent developments and partnerships. *Bulletin of the American Meteorological Society*, *92*(6), 704–708. <https://doi.org/10.1175/2011bams3015.1>
- Song, X. P., Hansen, M. C., Stehman, S. V., Potapov, P. V., Tyukavina, A., Vermote, E. F., & Townshend, J. R. (2018). Global land change from 1982 to 2016. *Nature*, *560*(7720), 639–643. <https://doi.org/10.1038/s41586-018-0411-9>
- Stjern, C. W., Samset, B. H., Boucher, O., Iversen, T., Lamarque, J. F., Myhre, G., et al. (2020). How aerosols and greenhouse gases influence the diurnal temperature range. *Atmospheric Chemistry and Physics*, *20*(21), 13467–13480. <https://doi.org/10.5194/acp-20-13467-2020>
- Sun, X., Ren, G., You, Q., Ren, Y., Xu, W., Xue, X., et al. (2018). Global diurnal temperature range (DTR) changes since 1901. *Climate Dynamics*, *52*(5), 3343–3356. <https://doi.org/10.1007/s00382-018-4329-6>
- Thorne, P. W., Donat, M. G., Dunn, R. J. H., Williams, C. N., Alexander, L. V., Caesar, J., et al. (2016). Reassessing changes in diurnal temperature range: Intercomparison and evaluation of existing global data set estimates. *Journal of Geophysical Research: Atmospheres*, *121*(10), 5138–5158. <https://doi.org/10.1002/2015JD024584>
- United Nations Department of Economic and Social Affairs, Population Division. (2022). World population prospects 2022: Summary of results. UN DESA/POP/2022/TR/NO. 3.
- Vasseur, D. A., DeLong, J. P., Gilbert, B., Greig, H. S., Harley, C. D., McCann, K. S., et al. (2014). Increased temperature variation poses a greater risk to species than climate warming. *Proceedings of the Royal Society B: Biological Sciences*, *281*(1779), 20132612. <https://doi.org/10.1098/rspb.2013.2612>
- Vose, R. S., Easterling, D. R., & Gleason, B. (2005). Maximum and minimum temperature trends for the globe: An update through 2004. *Geophysical Research Letters*, *32*(23), L23822. <https://doi.org/10.1029/2005GL024379>
- Wang, K., & Clow, G. D. (2020). The diurnal temperature range in CMIP6 models: Climatology, variability, and evolution. *Journal of Climate*, *33*(19), 8261–8279. <https://doi.org/10.1175/JCLI-D-19-0897.1>
- Wang, K., & Dickinson, R. E. (2013). Contribution of solar radiation to decadal temperature variability over land. *Proceedings of the National Academy of Sciences of the United States of America*, *110*(37), 14877–14882. <https://doi.org/10.1073/pnas.1311433110>
- Wang, X., Zhao, C., Müller, C., Wang, C., Ciais, P., Janssens, I., et al. (2020). Emergent constraint on crop yield response to warmer temperature from field experiments. *Nature Sustainability*, *3*(11), 908–916. <https://doi.org/10.1038/s41893-020-0569-7>
- Wang, Y., & Wild, M. (2016). A new look at solar dimming and brightening in China. *Geophysical Research Letters*, *43*(22), 11–777. <https://doi.org/10.1002/2016GL071009>
- Wild, M., Gilgen, H., Roesch, A., Ohmura, A., Long, C. N., Dutton, E. G., et al. (2005). From dimming to brightening: Decadal changes in solar radiation at Earth's surface. *Science*, *308*(5723), 847–850. <https://doi.org/10.1126/science.1103215>
- Wild, M., Ohmura, A., & Makowski, K. (2007). Impact of global dimming and brightening on global warming. *Geophysical Research Letters*, *34*(4), L04702. <https://doi.org/10.1029/2006GL028031>
- Williamson, M. S., Thackeray, C. W., Cox, P. M., Hall, A., Huntingford, C., & Nijse, F. J. (2021). Emergent constraints on climate sensitivities. *Reviews of Modern Physics*, *93*(2), 025004. <https://doi.org/10.1103/RevModPhys.93.025004>
- World Meteorological Organization (WMO). (2017). Guidelines on the calculation of climate normals (WMO-No. 1203). Retrieved from https://library.wmo.int/index.php?lvl=notice_display&id=20130
- Yang, S., Wang, X. L., & Wild, M. (2019). Causes of dimming and brightening in China inferred from homogenized daily clear-sky and all-sky in situ surface solar radiation records (1958–2016). *Journal of Climate*, *32*(18), 5901–5913. <https://doi.org/10.1175/JCLI-D-18-0666.1>
- Yang, Y., & Ren, R. (2017). On the contrasting decadal changes of diurnal surface temperature range between the Tibetan Plateau and southeastern China during the 1980s–2000s. *Advances in Atmospheric Sciences*, *34*(2), 181–198. <https://doi.org/10.1007/s00376-016-6077-z>
- Zhou, L., Dai, A., Dai, Y., Vose, R. S., Zou, C. Z., Tian, Y., & Chen, H. (2009). Spatial dependence of diurnal temperature range trends on precipitation from 1950 to 2004. *Climate Dynamics*, *32*(2), 429–440. <https://doi.org/10.1007/s00382-008-0387-5>
- Zhou, L., Dickinson, R. E., Dai, A., & Dirmeyer, P. (2010). Detection and attribution of anthropogenic forcing to diurnal temperature range changes from 1950 to 1999: Comparing multi-model simulations with observations. *Climate Dynamics*, *35*(7), 1289–1307. <https://doi.org/10.1007/s00382-009-0644-2>